Permeability of partially molten upper mantle rocks from experiments and percolation theory

Ulrich H. Faul

Research School of Earth Sciences, The Australian National University, Canberra, Australia

Abstract. Experiments with olivine and a basaltic melt were conducted to analyze the melt distribution in partially molten aggregates at low melt fractions. Grain size and melt distribution at the start of an experiment are transient; to reach steady state conditions requires run durations from 2 to 3 weeks at 1 GPa and 1300° to 1400°C. Quantitative analysis of the melt distribution from backscattered electron images of postrun samples shows that most of the melt resides in low aspect ratio, disk-shaped inclusions on two-grain boundaries at melt contents from 0.8 to 3.3 vol. %. Tubules along three-grain edges most likely interconnect the melt at all melt fractions, but their shape and size varies even at the lowest melt fractions due to the effects of anisotropy and nonuniform grain sizes. These triple junction tubules can therefore not be approximated by uniform, equally spaced cylinders with near constant cross-sectional area for the purpose of calculating the permeability of the matrix. Moreover, the tubules are much smaller than the disk-shaped inclusions; tubule-like geometries contain only ~ 10% of the total melt content in each experiment. The permeability of the triple junction tubule network only is therefore low (k ~ 10^{-17} m^2), and segregation velocities are less than 1 mm yr^{-1}. The permeability of the aggregate increases substantially only after the disk-shaped inclusions become interconnected. This melt fraction is calculated from percolation theory, using parameters of the melt inclusions obtained from the backscattered electron images. The threshold melt content, as calculated from the experimental melt distribution, lies between 2 and 3 vol. %.

Introduction

Melting induced by decompression of upwelling mantle or dehydration reactions initially takes place on a grain scale. Above ~200 km depth the melt is less dense than the solid matrix [e.g., *Agee and Walker*, 1988] and therefore buoyantly unstable. The ability of the melt to segregate from or percolate through the matrix and the velocity of the melt relative to the matrix depend on its intergranular distribution. Isolated pockets of melt will remain trapped, but if the melt is well interconnected by a regular array of nearly straight tubules it will segregate rapidly. Perfect interconnectivity of the melt is predicted for a partially molten aggregate with uniform, isotropic grains and a wetting angle between two grains and the melt that is smaller than 60° [e.g., *Bulau et al.*, 1979]. This model leads to relatively high permeabilities and rapid segregation even at low melt fractions (<10^{-2}) [e.g., *von Bargen and Waff*, 1986; *McKenzie*, 1989]. However, the melt distribution observed in long-duration experiments with upper mantle materials differs substantially from this idealized model. Instead of a regular array of melt-filled tubules along three-grain edges, images of experimental run products show most of the melt in thin and elongated inclusions, which can be approximated by oblate (disk-shaped) ellipsoids in three dimensions [*Faul et al.*, 1994].

One of the main reasons for the discrepancy between the melt distribution predicted by previous models and the experimentally observed melt distribution is the anisotropy of olivine surface energies. This anisotropy has been noted earlier [*Vaughan et al.*, 1982; *Cooper and Kohlstedt*, 1982, 1984], but the effects on the melt distribution have only been evaluated recently [*Bussod and Christie*, 1991; *Waff and Faul*, 1992; *Faul et al.*, 1994; *Hirth and Kohlstedt*, 1995a]. One particular aspect of anisotropic surface energies is the existence of some completely wetted or melt-separated two-grain boundaries for systems with a mean wetting angle larger than zero. As was pointed out by *Waff and Faul* [1992], only small variations in the ratio of solid-solid to solid-liquid surface energies are needed to cover the range of wetting angles from 0° (complete wetting of all grain boundaries) to 60° (pinch off). On the basis of data from *Cooper and Kohlstedt* [1982], *Hirth and Kohlstedt* [1995a] estimate that the variation of the olivine-basalt surface energy alone is large enough for some melt-filled two-grain boundaries. Melt-separated two-grain boundaries have also been reported by *Laporte* [1994] in long-duration, high-pressure, and temperature experiments with quartz and a granitic melt, even though quartz is much less anisotropic than olivine.

Owing to the effects of anisotropy and nonuniform grain size, measuring only wetting angles in a partially molten aggregate does not characterize the melt distribution sufficiently to predict bulk physical properties. Because of its intergranular distribution, the sizes and shapes of the melt inclusions are determined by the sizes, shapes, and relative orientations of neighboring grains. Therefore the melt distribution from an area that is large compared to the average grain size of a sample has to be evaluated to assess the interconnectivity of the melt as a function of melt fraction. To this end, piston cylinder experiments were conducted to

generate samples with low melt fractions ($\phi \leq 0.03$) as these are inferred for most partially molten regions of the upper mantle. For the melt distribution to be representative of upper mantle conditions it is necessary to run the experiments long enough so that the initial transient grain size distribution (the result of crushing and sieving of grain fragments) as well as a nonuniform distribution of the basalt powder due to incomplete mixing evolves to a steady state grain size distribution. Both grain growth and melt redistribution are driven by surface energy reduction. Since, contrary to the assumptions of the isotropic model, most of the volume of the melt resides in oblate (disk-shaped) ellipsoids, a permeability model is introduced that explicitly takes the observed melt inclusion shapes into account. To determine the threshold melt fraction at which the disk-shaped inclusions form an interconnected path and to calculate the permeability, percolation theory is introduced.

Experimental Conditions and Image Acquisition

All experiments were conducted in a solid medium piston-cylinder apparatus using graphite furnaces. The sample material is a mixture of olivine and basalt powder. The olivine grains were crushed and sieved to obtain the desired starting grain size range. Basalt powder was then mechanically mixed with each size fraction. The run conditions are summarized in Table 1. For run HD88 the starting material consisted of 98.5 wt % olivine from the interior of a dunite xenolith from Hualalai volcano, Hawaii, plus 1.5 wt % Hawaiian olivine basalt. Runs OB1 to OB11 had a starting composition of 95 wt % San Carlos olivine plus 5 wt % alkaline basalt; run OB23 had 99.5 wt % olivine hand-picked from a lherzolite xenolith from Mount Porndon, Victoria, Australia, plus 0.5 wt % synthetic basalt, similar in composition to the alkaline basalt. The sample material used in this study (except for OB23) is the same as that described by Waff and Faul [1992, Tables 1 and 2]; analysis of the prerun and postrun material and the establishment of chemical equilibrium are given there. Details of the starting material for OB23 will be given elsewhere (M. Cmiral et al., manuscript in preparation, 1997). Postrun examination of OB23 shows a distribution of small (<1 μm) graphite grains throughout the charge, which presumably are the residue of grinding the olivine under ethanol in an agate mortar. All sample material and furnace assembly parts were kept in a drying oven at 110° C for at least 24 hours prior to the run.

The furnace assembly of run HD88 had inner pieces and outer sleeves of soft-fired pyrophyllite and a high-purity iron sample capsule. A -15% friction correction to the pressure was applied. All other runs had inner pieces of crushable MgO and a graphite sample capsule, with an outer Pt capsule for run OB23 . Runs OB1 and OB2 had outer sleeves of pyrex glass and NaCl. A large increase of the current required to maintain constant temperature after about 24 hours was caused by molten glass penetrating into microcracks of the fine-grained graphite furnace at higher temperatures. Outer sleeves of CaF_2 alleviated this problem in runs OB10 and OB11. Al_2O_3 ceramic disks above and below the sample capsule prevented uneven deformation of it. The length of all parts was measured before and after each run to better than ±0.2 mm. No friction correction to the pressure was applied.

The temperature in all runs except OB23 was measured with W5%Re versus W26%Re thermocouples; no pressure correction to the thermocouple emf was applied. The temperature at the hot spot of the furnace was calculated from published thermal profiles [Boyd and England, 1963; Cohen et al.; 1967, Hudon et al., 1994], since the sample was centered on the hot spot and the thermocouple above it. Current and voltage across the furnace assembly were closely monitored and if drift occurred (due to oxidation of the W-Re thermocouple wires), the run was switched to constant power if it had been stable for at least 1 week. After this time, no further changes in the furnace assembly are expected, such that the previously set temperature was maintained to within ±10°-15°C (estimated uncertainty for the temperatures given in Table 1). Because of the oxidation of the W-Re thermocouple wires, type B Pt-6% Rh versus Pt-30% Rh thermocouples were used for run OB23. This type of thermocouple does not have the same degree of accuracy (particularly at lower temperatures) as type S Pt-Rh but does not oxidize or drift as type S does due to poisoning of the pure Pt leg. The power consumption of the furnace remained very stable over run duration of OB23. All runs were terminated by switching off the power to the furnace. The temperature dropped more than 300°C during the first second; the pressure dropped by about one third after 1 minute due to thermal contraction of assembly and apparatus. After the runs, the capsules were cut vertically through their centers, mounted in epoxy, and polished with diamond polishing compound to 0.25 μm. Run OB23 was polished with 0.05 μm alumina powder. As described by Faul et al. [1994], cracks in the sample from quenching are a problem for imaging of larger areas.

The back-scattered electron (BSE) images were obtained on a JEOL JSM 6300V scanning electron microscope (SEM) at the University of Oregon using an acceleration voltage of 10 kV and 8 mm working distance and beam currents of about 1 nA. The images for run OB23 were obtained on a JEOL 6400 SEM at the Australian National University, with an acceleration voltage of 15 kV and 15 mm working distance and a beam current of approximately 10 nA. Each image consists of 1024 by 1024 pixel with a grayscale resolution of 8 bits per pixel. The entire cross section of each sample was first imaged at low magnification to detect evidence of temperature gradients across the charge (which would cause a diffusive redistribution of the melt even if very small [Takahashi, 1986; Lesher and Walker, 1988]). The least fractured areas were selected for imaging at higher magnification from this map. The magnification chosen was a compromise between adequate resolution of small melt inclusions, particularly triple

Table 1. Experimental Conditions and Grain Sizes

Experiment[a]	Temperature, °C	Duration, hours	Starting Grain Size,[b] μm	Final Grain Size,[c] μm	Number of Grains
HD88	1350	549	45-62	66[d]	588
OB1	1300	24	45-62	n. d.[e]	—
OB2	1300	313	45-62	37	219
OB10	1300	381	<45	27	195
OB11	1310	424	62-75	28	222
OB23	1400	506	<25	n. d.	—

[a]The pressure of all experiments was 1 GPa.
[b]Grain size range before experiment from sieving.
[c]Apparent mean grain size after the experiment (see text).
[d]From Jung et al. [1992].
[e]Not determined (see text).

junctions and thin inclusions at two-grain boundaries, and the need to cover a large area to average out the effects of the grain size distribution on the melt distribution.

The 256 grayscale images were converted to binary images with only the melt remaining by digitizing the boundaries of the melt inclusions on screen. The combined effects of quench-cracks and the preferential removal of glass during polishing (producing topography on the sample surface and therefore varying grayscales of the glass, particularly affecting small inclusions) made automated thresholding impractical. No filtering was applied to either the grayscale or binary images. Sixteen images (in a 4 by 4 array) were analyzed from HD88 and 12 (in a 4 by 3 array) were analyzed from OB10 at a resolution of 7.4 pixel per μm. Parameters of melt inclusions extending across image boundaries were combined in results files before further processing. For further details of the image processing and discussion of the uncertainties, see *Faul et al.* [1994].

Experimental Results

Grain Size Distributions

The mean grain size in a polycrystalline aggregate at elevated temperatures (under hydrostatic conditions) increases over time, driven by the decrease in the system free energy, which results from the reduction in grain boundary area [e.g.; *Atkinson*, 1988]. As the mean grain size increases, grains above a certain size grow, while smaller grains decrease in size and eventually disappear. At the same time, a grain size distribution develops, which, when normalized by the mean grain size, is time invariant. The grain size distribution at the start of an experiment, the result of crushing and sieving of grain fragments, is transient and evolves toward the stationary distribution. Grain size distributions can therefore be used as an indicator whether a steady state grain growth regime has been reached. Since the driving force for this process, as well as for the distribution of the (intergranular) melt in the polycrystalline aggregate is the reduction of the surface energy of the system, a time invariant grain size distribution also means that the melt distribution is in a steady state.

Grain size distributions from four experiments and a lherzolite from Dreiser Weiher, Germany [*Jung et al.*, 1992] for comparison are shown in Figure 1. The grain sizes of the lherzolite and run HD88 were determined from thin sections, while those of runs OB2, OB10, and OB11 were determined from grain boundaries digitized from BSE images. In all cases the grain size was calculated from the average of the smallest and largest dimension of each grain in the plane of the section. The distributions shown in Figure 1 and discussed below therefore refer only to apparent values without three-dimensional correction [*Jurewicz and Watson*, 1985; *Laporte*, 1994]. Normalization by the (apparent) mean grain size emphasizes the relative nature of the distributions rather than the absolute value of the three-dimensional grain size.

The grain size distribution of run HD88 with the longest run duration is closest to distributions predicted for (steady state) normal grain growth [e.g.; *Anderson et al.*, 1989; *Jung et al.*, 1992]. The distribution is the most narrow of all runs, with few grains in the smallest size classes and a peak close to the mean grain size. The distributions of the lherzolite and run OB10 are somewhat broader but still have the peak of the distribution close to the mean grain size. The distributions of
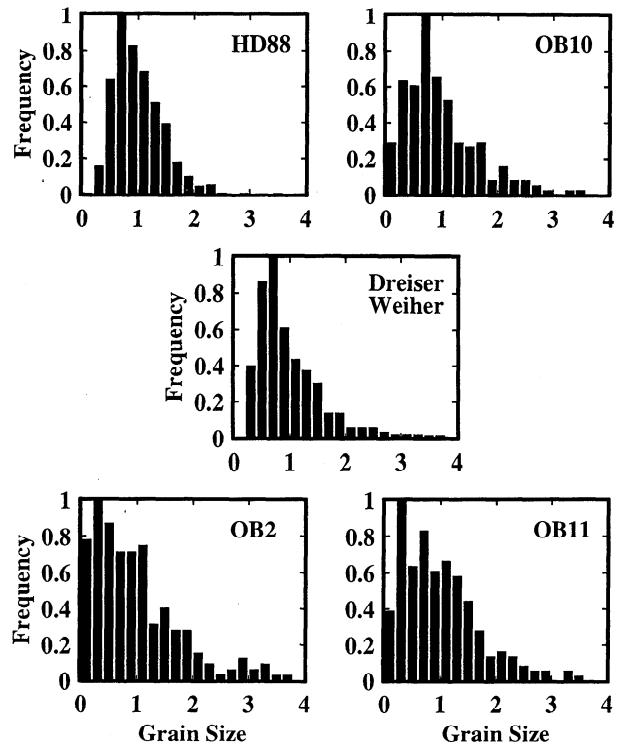
Figure 1. Histograms of the grain size distributions of four experiments and a lherzolite from Dreiser Weiher, Germany. The grain sizes are normalized by the mean grain size and plotted against the normalized frequency for better comparison of the distributions. The mean grain size and number of grains measured for the four experiments are given in Table 1, the (apparent) mean grain size of the lherzolite is 0.55 mm with 390 grains measured. The distribution of run HD88 with the longest run duration (~23 days) is the most narrow and has the peak close to the mean grain size. The distributions of the lherzolite and run OB10 (~16 days) are similar if somewhat broader. Runs OB2 (~13 days) and OB11 (~18 days) with larger starting grain sizes than OB10 have broader distributions with their peak close to the smallest grain sizes, indicating that these experiments have not yet evolved into a steady state grain growth regime. Since the melt resides at grain boundaries, the melt distribution also has not reached steady state. The data for the lherzolite and run HD88 were collected by *Jung et al.* [1992].

runs OB2 and OB11 in comparison are peaked at the smallest sizes and are broader, indicating that these runs have not yet developed into a steady state. Neither run was included in the permeability calculation and therefore the melt distributions were not further analyzed. Similarly, the grain size distributions of runs OB1 and OB23 were not determined. No abnormal grain growth (characterized by a few grains that are much larger than all others) was observed in any of the experiments.

Similar to the observations of *Hirth and Kohlstedt* [1995b], the estimated three-dimensional mean grain sizes (obtained by multiplying the apparent mean grain size by 1.5) are smaller than grain sizes predicted from growth rates of melt free, dry olivine aggregates [*Karato*, 1989]. One possible explanation for the different growth rates is that even a small melt fraction slows grain growth by acting as a secondary phase. The presence of faceted crystal-melt interfaces indicates that grain

growth rates are not limited by diffusion through the melt but the kinetics of the surface reactions [see *Waff and Faul*, 1992, and references therein]. The time required to reach steady state can therefore not be calculated from diffusion coefficients and distances in the melt.

Description of the Melt Distribution

Images of the experimental charges after 1 day (run OB1, Figure 2), 2 weeks (OB10, Figures 3 and 4), and more then 3 weeks (HD88) show the evolution of the melt distribution over time. OB1 has a number of large melt pools (Figure 2), which are due to the incomplete mixing of the olivine and basalt powders before the run. Numerous small grain fragments are present, which have not yet started to recrystallize. The large melt pools also enable more grains to grow with their ideal crystal habits, resulting in a larger number of flat faces. In comparison, the melt distribution in runs OB10 and HD88 with melt contents of 2.5 vol. % and 1 vol. %, respectively, is more homogeneous; larger, more equant melt inclusions do not exceed the size of the smallest grains.

Even though the melt in runs OB10 and HD88 is more evenly distributed over the whole charge, the melt distribution on a grain scale cannot be described by a regular array of intergranular melt inclusions. Some areas contain relatively little melt, while others have higher melt fractions, mainly associated with smaller grains (Figure 3). The melt inclusions vary in size and shape, with larger and more equant inclusions frequently surrounded by four grains. Some of these larger inclusions can be due to shrinking grains, which will eventually disappear, while others grow around them. Characteristic triple junctions (e.g., near the top of Figure 3) are typically small compared to other melt inclusions. Most two-grain boundaries are melt free (and are not visible in these BSE images), but most of the melt is contained in thin melt inclusions (Figures 3 and 4). Figure 4 shows an area with an above average melt fraction and a relatively high concentration of melt inclusions less than 1 μm wide. A comparison of Figures 3 and 4 from OB10 with Figure 2 from OB1 also indicates that the melt-filled two-grain boundaries are the result of textural evolution during grain growth, as there are very few present in OB1 with a similar melt fraction as OB10.

Figures 5 and 6 show BSE images from HD88 and OB10 at higher magnification. These images emphasize two points: the effects of grain growth on the shape and size of the melt inclusions and the varied shape and size of triple junction tubules. During grain growth, simultaneous growth and shrinkage of individual grains will always lead to nonideal grain boundary configurations. These nonideal configurations drive further growth [e.g., *Atkinson*, 1988; *Anderson et al.*, 1989] and concomitant redistribution of the melt which fills intergranular spaces. Figures 5a and 5b illustrate that during growth, crystalline grains try to achieve an ideal crystal habit
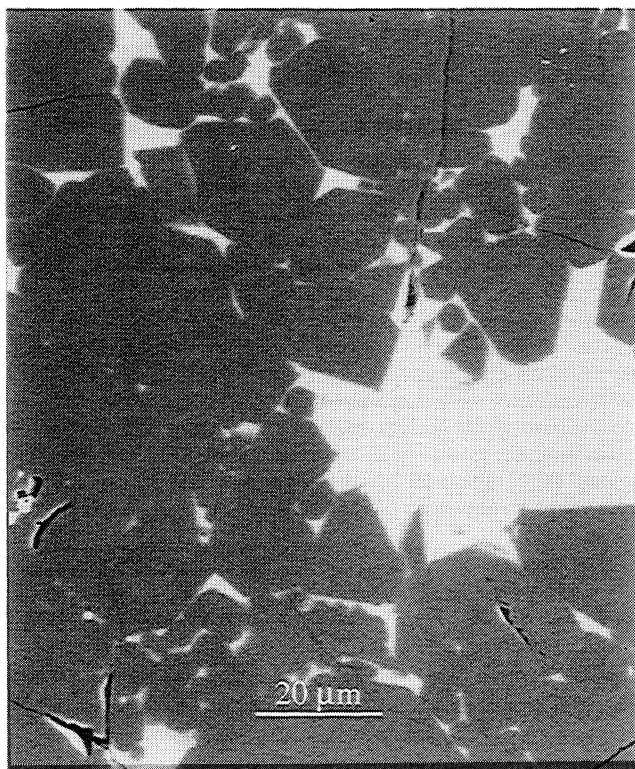
Figure 2. Backscattered electron (BSE) image from run OB1 with a duration of 24 hours, showing melt and grain size distributions that have not reached steady state. Glass appears light grey; olivine is darker. Black features are cracks from quench and postrun sample preparation. Several features are worth noting: The large melt pool (in comparison to the grain size) is a remnant of incomplete mixing of the olivine and basalt powders prior to the run. Large melt pools allow uninhibited growth of individual olivine grains with faceted crystal-melt interfaces. Numerous small grains and grain fragments are present, which have not recrystallized from grinding prior to the run and crushing during pressurization.
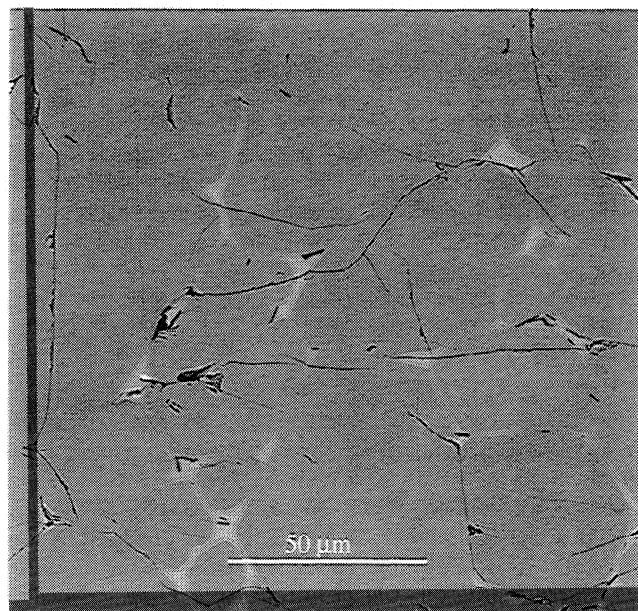

Figure 3. BSE image from run OB10, which has reached steady state. No melt pools that are large in comparison to the grain size are present in this run; the melt is relatively homogeneously distributed over the charge. Recrystallization and grain growth together with surface energy minimization of crystal-melt interfaces lead to redistribution of the melt from the initial transient distribution. The melt fraction remains variable on the scale of individual grains, with smaller grains commonly having a higher associated melt fraction. Flat crystal-melt interfaces are visible at this scale but less prevalent than in Figure 2. Faint straight lines are from polishing with diamond compound.
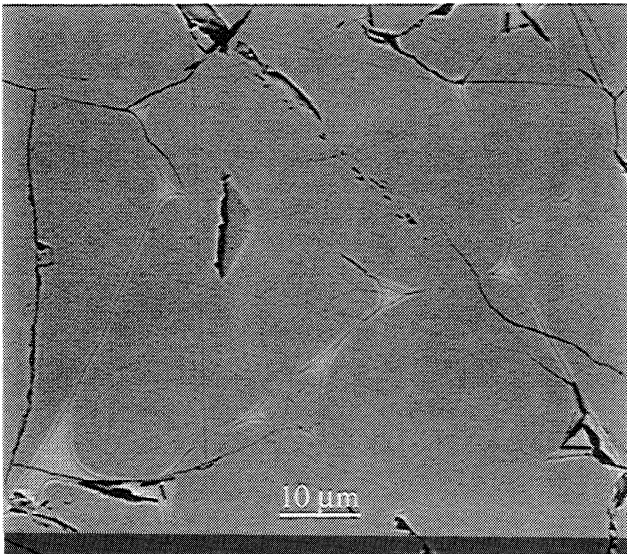
Figure 4. BSE image from run OB10. This image shows an above average melt fraction for this run and a high concentration of thin melt inclusions on two-grain boundaries. In comparison, OB1 (Figure 2) has fewer melt-filled two-grain boundaries, indicating that these features are produced during the experiment as a result of surface energy minimization.

but are restricted by neighboring grains. Arrows in Figure 5b indicate quench growth features at the intersection of slow growing flat faces with faster growing rounded ones. These quench growth features are too small to alter the melt inclusion shapes. Figures 6a and 6b show examples of different shapes of triple junction tubules due to anisotropy effects; Figures 6c and 6d illustrate their range of sizes. A comparison of Figure 4 and Figures 6c and 6d, all from OB10 at similar scales, shows the variability of the local melt fraction and the trend toward an increase in the number of melt-filled two-grain boundaries with increasing melt fraction.

Orientation contrast images from OB23 (Figure 7) indicate that even at a melt fraction of about 0.001 the melt does not reside in a uniform network of triple junction tubules of equal size. In comparison to the melt distribution at higher melt fractions (runs HD88 and OB10) triple junction tubules do contain a higher proportion of the total melt content, but because the few scattered low aspect ratio melt inclusions are again much larger than most triple junction tubules (Figure 7a), they contain a significant proportion of the total melt fraction. The triple junction tubules also show a range in sizes, the smallest can barely be resolved by BSE imaging (Figure 7b). Examination by transmission electron microscopy shows that some are as small as 20 nm in diameter (M. Cmiral et al., manuscript in preparation, 1997). The presence of a melt-free three-grain edge can be inferred for the
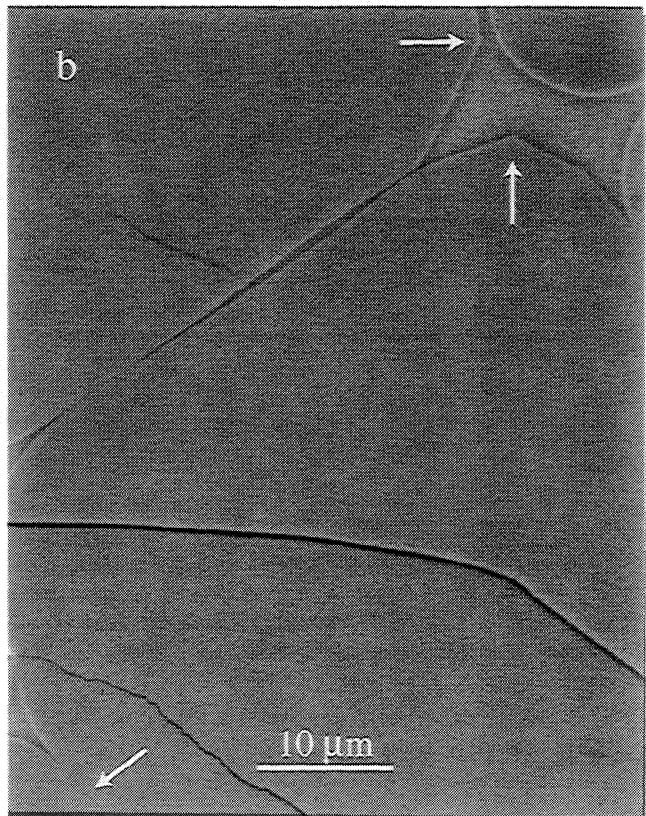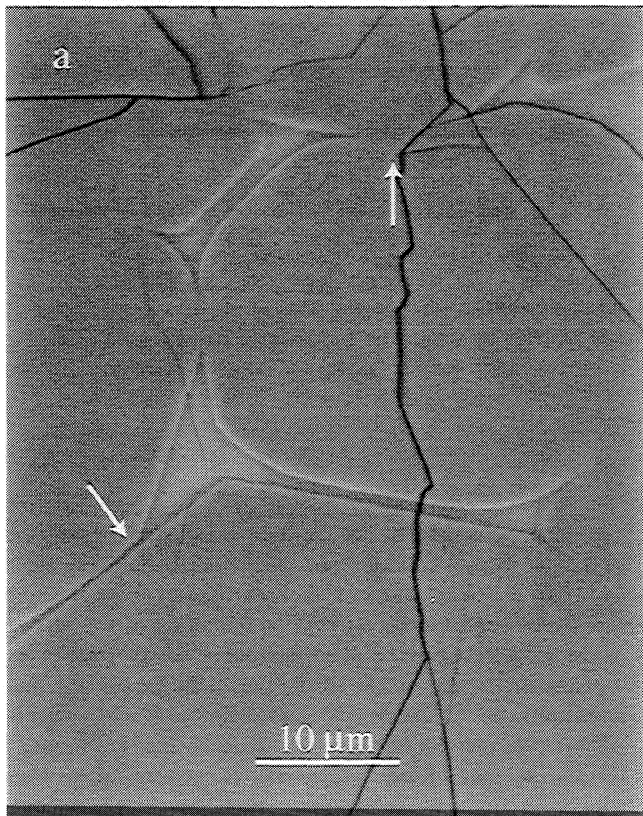
Figure 5. BSE images from run HD88 with a run duration of 550 at 1350°C and 1 GPa showing details of grain and melt inclusion shapes. (a) Topological instabilities such as the concave grain boundary indicated by the arrow near the top of the image develop during steady state grain growth as some grains shrink and others grow to fill their space [see *Atkinson*, 1988, and references therein]. During this process, individual crystals tend to develop their ideal shape but are restricted in their growth by neighboring grains (arrow near left edge). (b) The transition from slow growing, flat crystal-melt interfaces to faster growing rounded ones is marked by small quench growth features (arrows near the top right corner of the image). The trace of a melt film at the resolution limit of BSE imaging is indicated near the bottom left corner. Note the ellipsoidal melt inclusion in the center part of the image.
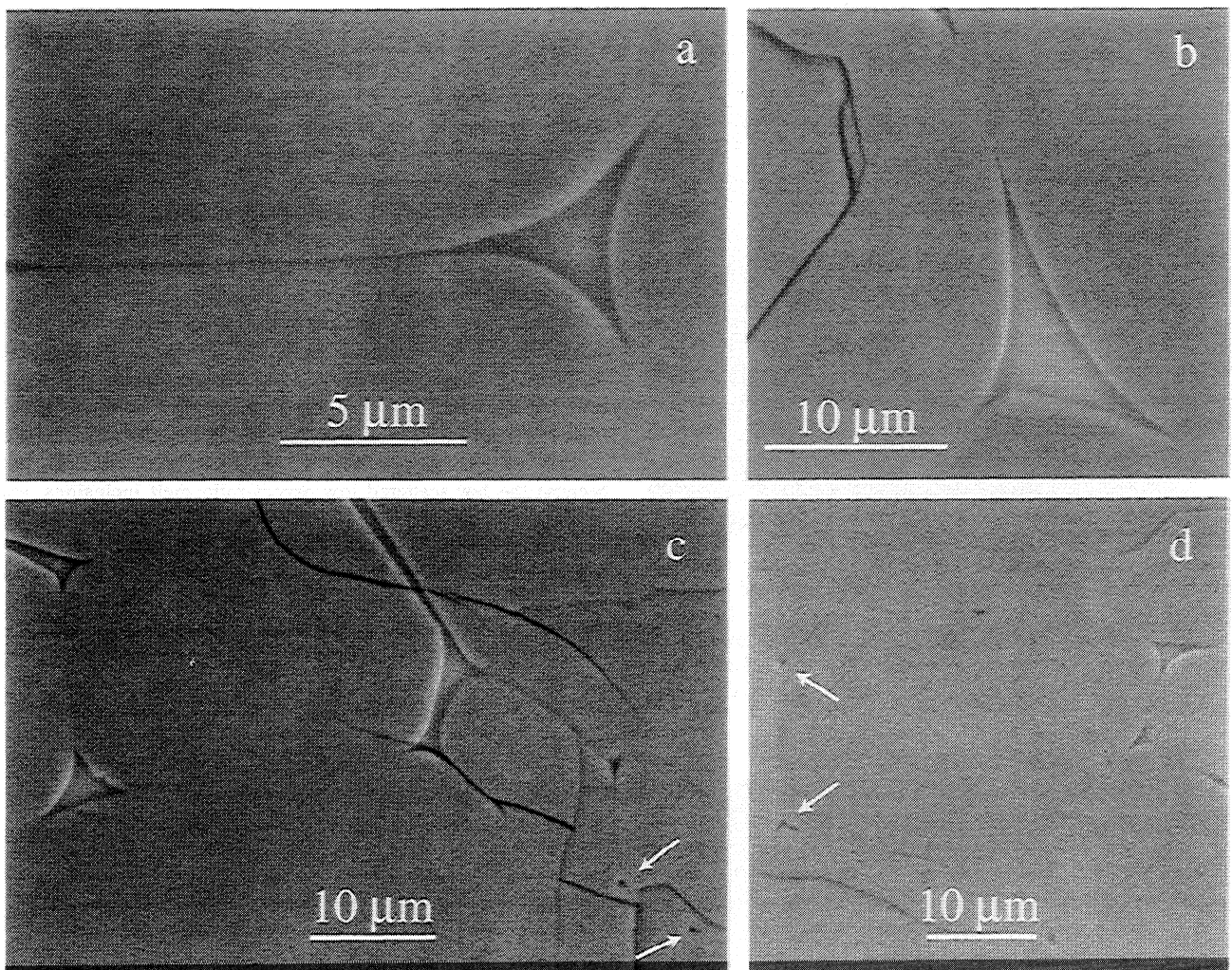
Figure 6. Examples of triple junction tubule geometries from run HD88 (Figures 6a and 6b) and OB10 (Figures 6c and 6d). Note the difference in scale in comparison to Figure 3. (a) Nearly ideal cross section of a triple junction tubule except that the wetting angle is equal to zero at one of the two-grain boundaries involved. The other grain boundaries are melt free. (b) Triple junction tubule that is flattened in one direction probably due to the flat crystal-melt interface in conjunction with small wetting angles at the other corners. (c) and (d) Images illustrating the range in size of the triple junction tubules, from less than 1 μm to ~6 μm in these images. The arrows point to small triple junction tubules.

center of Figure 7c; alternatively, one of the grain boundaries involved might be a subgrain boundary. However, the formation of isolated, angular melt pockets at four-grain corners (which would leave all three-grain edges melt free) requiring a threshold melt fraction for interconnection of anisotropic systems [*Laporte and Watson*, 1995] is not observed.

Analysis of the Melt Distribution

The quantitative analysis of the melt distribution was carried out from binary images such as Figure 8 by image-processing software (Dapple Image Set, NIH Image (public domain program, developed at the U.S. National Institutes of Health and available on the Internet at http://rsb.info.nih.gov/nih-image/)). The grayscale range representing melt in Figure 3 is black; all else is white. The independent parameters area, perimeter, length (the longest chord connecting any two points on the perimeter), and the center of gravity (in the plane

of the image) of each individual inclusion were determined from these binary images. The derived parameters width and fiberlength were calculated from the independent parameters. The further characterization of the melt inclusions is given in more detail by *Faul et al.* [1994]. In particular, it was shown that the melt inclusions can be approximated by ellipses in two dimensions and oblate (disk-shaped) ellipsoids in three dimensions.

The aspect ratios α (the ratio of the minor axis to the major axis of an ellipse) of the melt inclusions were calculated from the ratio of width to fiberlength. Both parameters are best suited to describe thin and elongated features [*Russ*, 1990]. Figure 9 shows histograms of the distribution of the melt by aspect ratio and area of runs OB10 and HD88. The total number of inclusions measured was 254 for OB10 and 166 for HD88. As was the case for the experiments reported by *Faul et al.* [1994], the distribution of melt by aspect ratio is skewed toward low aspect ratio inclusions (Figures 9a and 9b). The distribution by aspect ratio and area shows that most of the
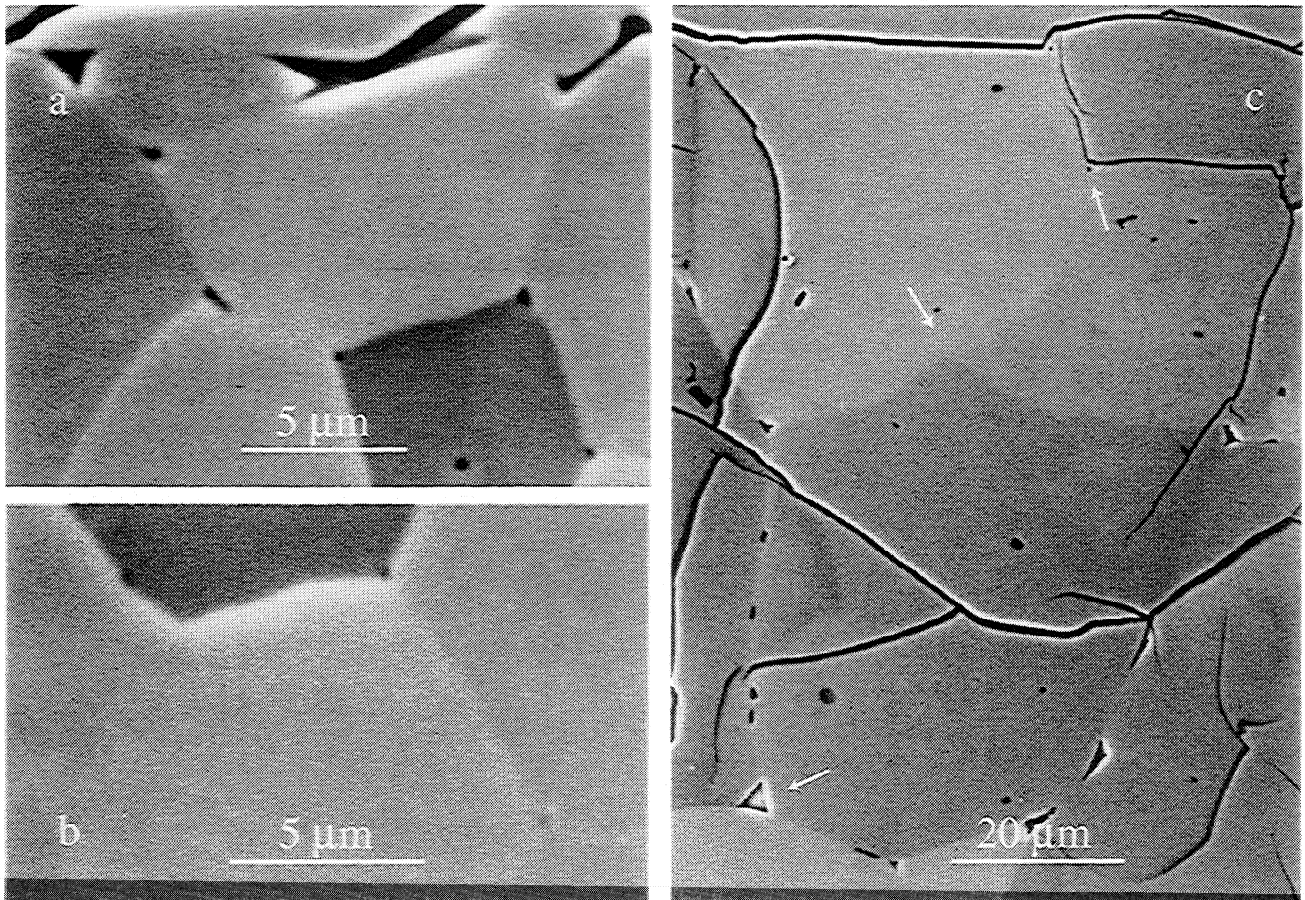
Figure 7. BSE images from run OB23 with a melt fraction of approximately 0.001. These images were acquired with a higher electron beam current than Figures 2-6. Together with a high quality polish olivine shows orientation contrast, making grain boundaries visible, but also accentuating cracks and topographic effects a the edges of melt inclusions. (a) Despite the low overall melt fraction, melt geometries other than triple junction tubules are present (faceted melt inclusions near the top of the image) and contain a significant amount of the total melt fraction. (b) The presence of some triple junction tubules in this image can only be inferred from a few dark pixel. (c) This image shows the size range of the triple junction tubules, a small and a large tubule are indicated by arrows. At the three-grain edge in the center (indicated by an arrow) no melt can be detected with BSE imaging; however one of the grain boundaries involved could be a subgrain boundary, which are more commonly melt free. The black inclusions on two-grain boundaries and grain interiors are small graphite grains, most likely the residue from grinding the olivine in ethanol.

volume of the melt resides in low aspect ratio inclusions (Figures 9c and 9d). This confirms that triple junction tubules, with $\alpha \geq 0.2$, only contain a small amount of melt.

To calculate the interconnectedness and permeability of ellipsoidal inclusions, the parameters length, width and spacing are needed. While the fiberlength gives the length of an elongated, curved inclusion when it is projected onto a straight line [see *Russ*, 1990, Figure 7-16], the length of an inclusion is used for the calculation of the probability that two neighboring inclusions overlap. The spacing of the melt inclusions was determined from the minimum of the distances of the center of gravity of each melt inclusion to all others (i.e., the distance to the nearest neighbor of each melt inclusion).

Figure 10 and Table 2 indicate the distributions of these parameters for runs HD88 and OB10. The peak in the distribution of lengths of all melt inclusions (Figures 10a and 10b) below 10 µm contains mostly triple junction tubules. Inclusions on two-grain boundaries are longer and less

numerous and stretch over several grains in some cases. The subset of triple junction tubules only in Figures 10c and 10d show that they are not uniform in size, ranging from less than 1 µm to 10 µm. The nearest neighbor distances (Figures 10e and 10f) have an almost normal distribution. The range over 2 orders of magnitude of the length and distances of all inclusions reflects the range of grain sizes, since the inclusions are located at grain boundaries. In comparison, the widths of the inclusions have a much smaller range than the other two parameters (Table 2).

Comparison of Permeability Models

The permeability of partial melts is commonly determined by making a number of simplifying assumptions about the melt distribution. The most important assumptions are regular, symmetric (spherical or tetrakaidekahedral) grains of equal size with isotropic surface energies [*Frank*, 1968; *Maaløe and Scheie*, 1982; *von Bargen and Waff*, 1986]. In textural
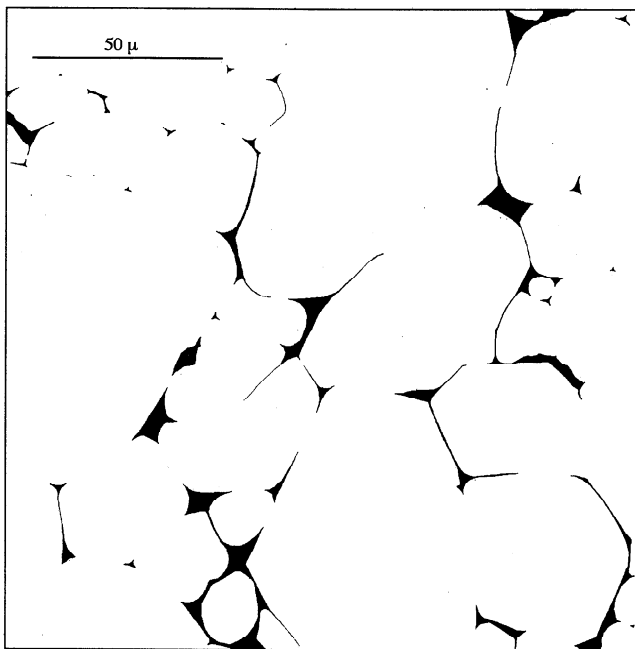
Figure 8. Binary image showing the same area as Figure 3. The melt fraction in this image is 2.9 vol. %, the average melt fraction from all images of this run is 2.5 vol. %. The independent parameters describing each melt inclusion are determined from these images with the help of image-processing software.

equilibrium the crystal-melt interfaces have constant mean curvature, and the melt is confined to tubules along three-grain-edge intersections and four grain corners [e.g., Beere, 1975; Bulau et al., 1979], forming a completely regular network of
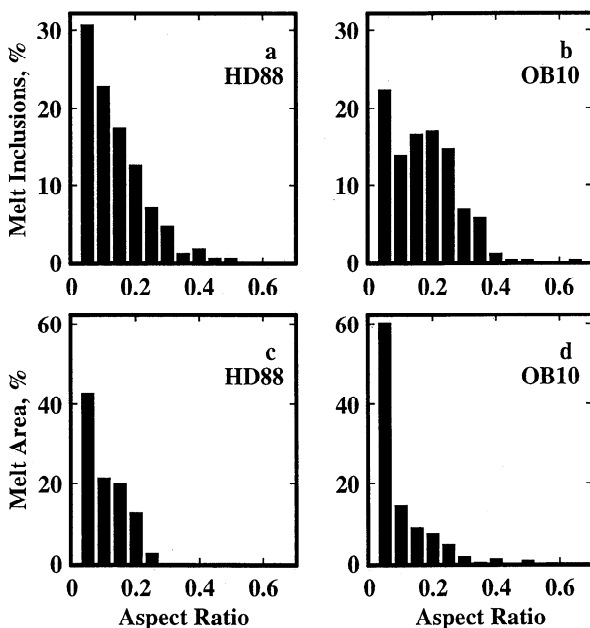
Figure 9. Histograms of the melt distribution from runs HD88 and OB10 with melt contents of 1 vol. % and 2.5 vol. %, respectively. (a) and (b) Melt distribution by aspect ratio as percentage of the total number of melt inclusions from all images of each run. (c) and (d) Melt distribution by aspect ratio and area as percentage of the total melt area of each run. As in the two previously described experiments [Faul et al., 1994], most of the melt resides in low aspect ratio inclusions with a pronounced peak at $\alpha = 0.05$.
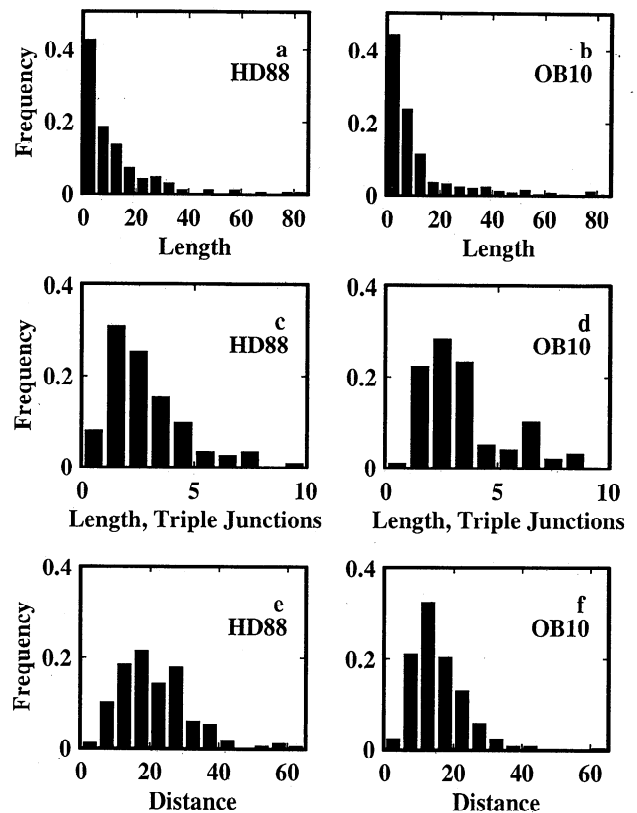
Figure 10. Histograms of melt inclusion parameters. (a) and (b) The peak in the length of all melt inclusions below 10 μm contains mostly triple junction tubules. The longest inclusions are the low aspect ratio, disk-shaped inclusions. (c) and (d) Triple junction tubules only still have a range of lengths from less than 1 μm to 10 μm. (e) and (f) Distribution of the nearest neighbor distances. The wide range in length and distances reflects the range of grain sizes present in these experiments. All parameters are given in μm.

identical channels (i.e., a melt channel along each three-grain edge intersection). Given the wetting angle (the contact angle between two crystalline grains and the melt) and the melt fraction, the melt geometry can be uniquely determined [von Bargen and Waff, 1986].

The permeability k for this model is calculated similarly to that of an array of cylindrical tubes [e.g., Turcotte and Schubert, 1982], with a correction factor (C) that takes the specific channel geometry into account:

$$k = \frac{d^2 \phi^n}{C} \qquad (1)$$

Table 2. Melt Inclusion Parameters

	HD88			OB10		
	Length	Width	Spacing	Length	Width	Spacing
			All Inclusions			
Maximum	81.3	9.8	63.8	82.8	5.9	61.4
Minimum	0.7	0.1	4.0	0.7	0.2	3.1
Mean	11.8	1.2	21.0	11.8	1.4	15.6
			Inclusions With $\alpha < 0.15$			
Mean	15.6	1.2	26.1	21.3	1.6	26.5

All dimensions are given in micrometers.

The parameter d represents the grain diameter (or more generally the channel spacing); ϕ represents the melt fraction. In this model the permeability is a continuous function of the melt fraction; for melt fractions below 0.03 an exponent n = 2 is predicted, as for Poiseulle flow in cylidrical tubes [e.g., *von Bargen and Waff*, 1986; *Stevenson*, 1986; *Stevenson and Scott*, 1991; *McKenzie*, 1989]. A characteristic feature of this model is that in addition to controlling the flow the tubes or cylinders also contain all or most of the melt fraction. A change in melt fraction is accommodated by changing the tube diameter; the overall geometry does not change.

Experimentally observed relationships between permeability and porosity for a wide range of materials from sandstones [*Bourbie and Zinszner*, 1985; *Doyen*, 1988], calcites [*Zhang et al.*, 1994], and ceramics and metals [*Kingery*, 1963] are best fit by an exponent n = 3 for porosities well above the residual porosity, where the material becomes impermeable. The pore space in these materials is generally heterogenous, with a wide range of pore sizes and shapes. Flow calculations for special geometries, for example, the intersection of two cracks or a crack and a tube, will only yield different geometrical constants but cannot account for the measured exponents or a change in pore geometry with porosity. Models attempting to reproduce the observed behavior are based on a macroscopic description of the pore space rather than considering individual geometries. One class of models, termed equivalent channel models, account for the heterogeneity of the pore structure by introducing the concept of hydraulic radius and tortuosity [e.g., *Walsh and Brace*, 1984; *Paterson*, 1983]. These models are also based on Poiseulle flow through cylindrical tubes, but the tube radius is replaced with an hydraulic radius. The hydraulic radius is defined as the ratio of pore volume to wetted area; the tortuosity is the actual path length relative to the apparent path length [see *Walsh and Brace*, 1984, Figure 1]. From this model *Walsh and Brace* [1984] derive a cubic dependence of permeability on porosity.

Lockner and Evans [1995] employ a different model to reproduce the variation in conductivity with porosity in an aggregate of hot-pressed quartz with water as pore fluid. Their model consists of a regular network of tubes with spheres at their intersections. The radius of the tubes and spheres decreases by the same amount with decreasing porosity, but the spheres increasingly dominate the pore volume until only a residual porosity in (unconnected) spheres remains. The calculated exponent n (equation (1)) is 3.8 (well above the residual porosity), even though the flow is controlled by cylindrical tubes and the pore space remains completely interconnected. The difference to the above models with cylinders only is the change in style of the pore volume from dominantly spheres at low porosities to tubes contributing increasingly to the total porosity.

In contrast to the assumptions of the isotropic model of the melt distribution, but similar to the porous materials referred to above, the melt in experimental charges is inhomogeneously distributed, and the shape and size of the individual melt inclusions varies greatly (Figures 3-7, Table 2). As shown in the previous section, the reasons are the range of grain sizes due to grain growth and surface energy anisotropy. In the experiments discussed here and by *Faul et al.* [1994] most of the melt resides in geometries that can be approximated by disk-shaped ellipsoids. Geometries similar to those expected for triple junction tubules are present in all experiments, but the melt fraction in the triple junction tubule-like geometries

only in these four experiments (HD87, HD88, BL82, and OB10) is about 10% of the total melt fraction (Table 3). In addition, the triple junction tubules are not uniform in size and shape (e.g., Figure 6). Figures 10c and 10d show histograms of the maximum dimension in the plane of the section of the triple junction tubules (i.e., the length as defined above) of runs HD88 and OB10. The distributions are similar in both runs and range over more than 1 order of magnitude. Small grains typically have an above average melt fraction associated with them (Figure 3), and accordingly, the triple junction tubules there have a much higher curvature along axis as compared to the triple junction tubules associated with large grains. The curvature of individual tubules is not constant if low energy (flat) grain boundaries are involved.

For partially molten rocks therefore a change in melt fraction is not simply accommodated by varying the tubule diameter, leaving the overall geometry unchanged; rather, the style of the melt geometry changes by increasing the number of melt-filled two-grain boundaries with increasing melt fraction, while the melt fraction in triple junction tubules (and therefore their diameter) increases only very slowly. However even at melt fractions on the order of 0.001 some disk-shaped inclusions are present (Figure 7), containing a significant fraction of the total melt content. The smallest tubules at this melt fraction may no longer contribute to the flow, as surface effects become increasingly important [*Hess*, 1994], reducing permeability further.

The effect of increasing n from 2 to 3 in the permeability-porosity relationship (equation (1)) can be illustrated by calculating the segregation velocity of melt from a stationary matrix following *McKenzie* [1989] using the values given there:

$$V_m = \frac{k \, \Delta\rho \, g}{\phi \, \mu} \qquad (2)$$

Here $\Delta\rho$ is the density difference between matrix and melt, g is the gravitational acceleration, and μ is the viscosity of the melt. At a melt fraction of 0.001 (the fraction of melt in triple junction tubules at a total melt fraction of 0.01) the segregation velocity decreases from 5 mm yr^{-1} with n = 2 and C = 3000 to 0.16 mm yr^{-1} with n = 3 and C = 100, leaving all other parameters constant (grain size, 10^{-3} m; density difference between melt and matrix, 500 kg m^{-3}; melt viscosity, 10 Pa s). With n = 3 a melt fraction of 0.08 is required before the segregation velocity reaches meters per year. Since n = 2 is predicted only for models where the pore space consists mostly of regular, uniformly varying tubes at all melt fractions, whereas partial melts involve a heterogeneous pore space with two different geometries (approximated by disks and tubules) of varying relative proportions, the permeability at small melt fractions is much lower than predicted by the isotropic model of the melt distribution. If similar to the behavior observed for crustal

Table 3. Melt Fractions

Experiment	Total Melt Fraction[a]	Melt Fraction in Triple Junction Tubules[a]
HD87	0.008	0.0009
HD88	0.010	0.0011
OB10	0.025	0.0014
BL82	0.033	0.003

[a]Averaged from all images of each experiment.

rocks, the exponent increases as melt fractions become very small (assuming the residual porosity is equal to zero); the permeability will be lower again. Both anisotropy and nonuniform grain size will influence the melt distribution in the upper mantle, implying that melt does not segregate as rapidly as predicted from models assuming crystalline isotropy.

Permeability Model for Disk-Shaped Melt Inclusions

The discussion above suggests that a permeability model for partially molten rock is needed that takes the particular melt geometry into account. *Dienes* [1982], *Gueguen et al.* [1986], *Gueguen and Dienes* [1989] and *Engelman et al.* [1983] have introduced models for ellipsoidal cracks that are best suited to account for the observed melt inclusion shapes. An important difference between this approach and the isotropic model is that the ellipsoidal melt inclusions by themselves do not automatically form an interconnected network. A rock containing (only) randomly spaced and oriented cracks is not permeable unless enough cracks overlap to form a connected path across the entire volume of interest. *Gueguen et al.* [1986] use this model to calculate the permeability of a sample of Fontainebleau sandstone with a mixture of pores and grain-boundary cracks; the calculated permeability matches the experimentally measured permeability very well. *Charlaix et al.* [1987] point out that for fracture networks with wide distributions of conductances the macroscopic permeability is controlled by the weakest bonds among the good ones necessary to ensure interconnection. Here the tubules, which constitute the weaker but interconnected set of bonds, control the permeability in the absence of a set of disks which by themselves form an interconnected path.

The calculation of the permeability for the ellipsoidal melt inclusions (disks) involves two parts: the fluid flow through individual disks and interconnection of the disks. To determine the interconnection of the disks, the concepts of percolation theory are used. In the following sections some main aspects of percolation theory are introduced as they apply to the situation considered here. For a general introduction to percolation theory, see, for example, *Stauffer and Aharony* [1992].

Percolation Theory

Percolation theory characterizes the behavior of an (infinite) set of bonds that are randomly occupied with probability p. The number of bonds leaving a site is the coordination number z. For fluid to flow between two neighboring sites the bond between the two sites has to be occupied. In the case considered here the crystalline grains are randomly oriented, and only certain relative orientations of adjacent grains favor melt between them. Two melt inclusions have to intersect to form a bond. The probability for intersection increases with increasing melt fraction, or equivalently, connected sites form clusters which increase in size as p increases. The problem then is to find the critical probability p_c for the onset of percolation, at which an (infinite) cluster first extends across the entire volume of interest. This problem can be treated analytically if one assumes a particular lattice structure, the Bethe lattice, which continuously branches but has no closed loops [e.g., *Stauffer*

and Aharony, 1992, Figure 9]. The critical probability depends on the coordination number and can be calculated from [*Fisher and Essam*, 1961; *Stauffer and Aharony*, 1992]

$$p_c = \frac{1}{z-1} \tag{3}$$

For other lattices, (2) becomes an inequality $p_c > 1/(z-1)$, but the exact value can only be determined numerically.

The probability for two disks (melt inclusions) to intersect (equivalent to the bond occupation probability) is calculated from the spacing of the disks, the coordination number and the excluded volume (defined as the volume surrounding the center of an object in which a second object must lie in order for the two objects to intersect [*de Gennes*, 1976]). The average excluded volume for a pair of disks of random orientation and radius r is $V_{ex} = \pi^2 r^3$. For disks with a range of radii, V_{ex} is calculated from [*Charlaix et al.*, 1984]:

$$V_{ex} = \pi^2 \overline{r^3} \tag{4}$$

where the bar indicates the mean. Because the distribution of lengths (equal to 2r) of the melt inclusions in Figure 10a and 10b is not Gaussian, $\overline{r^3}$ cannot be replaced by $\bar{r}^3$. The probability for two melt inclusions to intersect is calculated from [*Gueguen and Dienes*, 1989]:

$$p = \frac{1}{z} \frac{V_{ex}}{\overline{d^3}} \tag{5}$$

where $1/\overline{d^3}$ is the number of disks per unit volume. A similar result (except for the factor 1/z) was obtained in two dimensions by *Engelman et al.* [1983] for a continuous distribution of crack positions, that is, without assuming a particular lattice. Other continuum models, such as "Swiss cheese" models, where spherical, nonconducting holes are randomly placed in a conductive medium [e.g., *Halperin et al.* 1985], lead to too high values for the coordination number for the ellipsoidal inclusion shapes considered here. Since the coordination number cannot be determined independently, z = 4 is chosen, following *Dienes* [1982] and *Gueguen and Dienes* [1989].

Application to Partial Melts

Before calculating the intersection probability and permeability, the assumption that the melt inclusions can be best approximated by an oblate as opposed to a prolate shape can be verified. For this purpose the melt fraction is calculated from the parameters length, width, and spacing for oblate and prolate ellipsoids and compared to the melt fraction directly obtained from the binary images (by automatic counting of the fraction of black pixel of the total image area). The melt fraction for ellipsoidal disks with a half crack aperture w is [*Gueguen and Dienes*, 1989]:

$$\phi = 2\pi \frac{\overline{r^2 w}}{\overline{d^3}} \tag{6}$$

In Figures 11a and 11b the melt fraction calculated from (6) is plotted against the cumulative aspect ratio α_{cut}, where α_{cut} indicates that the melt fraction is calculated from the sum of those inclusions with $\alpha < \alpha_{cut}$. The calculated melt fraction is somewhat too high if all melt inclusions are used for the calculation (i.e., $\alpha_{cut} > 0.23$ for OB10). High aspect ratio inclusions are poorly represented by disk-shaped ellipsoids, including triple junction tubules with $\alpha \sim 0.2$. If only inclusions with $\alpha < 0.15$ are used, the calculated melt fraction
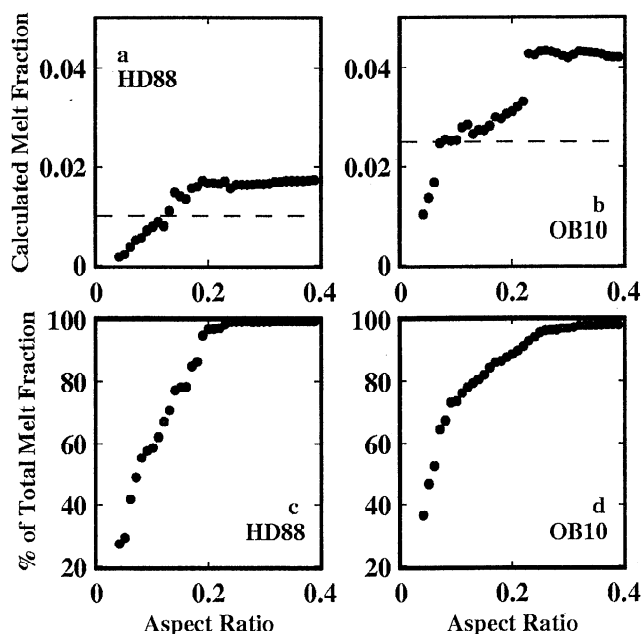
Figure 11. (a) and (b) Melt fraction calculated for disk-shaped ellipsoids plotted against the cumulative aspect ratio α_{cut}. All inclusions with an aspect ratio < α_{cut} are used to calculate the melt fraction at the aspect ratio α_{cut}. The melt fraction determined from the average of all images of each run is indicated by the dashed line. (c) and (d) Cumulative melt

is close to the melt fraction determined from the average of all binary images of each run while accounting for 80% of the melt (Figures 11c and 11d). In comparison, for prolate (cigar-shaped) ellipsoids, the melt fraction ϕ is proportional to $\overline{r\,w^2}$. The calculated melt fraction at $\alpha_{cut} = 0.15$ is then more than 1 order of magnitude too small for both runs.

The probability of intersection from (5) plotted against the cumulative aspect ratio α_{cut} is shown in Figure 12 for HD88 and OB10 (this study) and HD87 and BL82 [Faul et al., 1994]. Runs HD87 and HD88 with 0.8 and 1 vol. % melt, respectively, are well below the critical value for the onset of percolation (p_c = 1/3 for z = 4), even if all inclusions are used for the calculation. OB10 and BL82 with 2.5 and 3.3 vol. % melt are above the percolation threshold for $\alpha_{cut} > 0.1$; that is, the low aspect ratio inclusions form a connected cluster at this melt fraction.

The permeability for randomly spaced ellipsoidal inclusions is calculated from [Dienes, 1978, 1982, Gueguen and Dienes, 1989]

$$k = \frac{4\pi}{15}\frac{\overline{w^3 r^2}}{\overline{d^3}}f \qquad (7)$$

Again, Engelman et al. [1983] arrive at the same result for their continuum model except for a different numerical factor. The factor f represents the interconnectivity of the inclusions and is obtained from percolation theory. It is equal to zero (and therefore k = 0) if the intersection probability p is smaller than the critical probability p_c and is equal to one for p = 1 (all bonds occupied). Just above the percolation threshold, only one cluster exists that extends across the medium. This (infinite) cluster has many dead ends (dangling bonds). Only the fraction of disks that belong to the percolation backbone of this cluster (i.e., all dangling bonds are erased), contributes to the permeability. The factor f near p = p_c is determined from
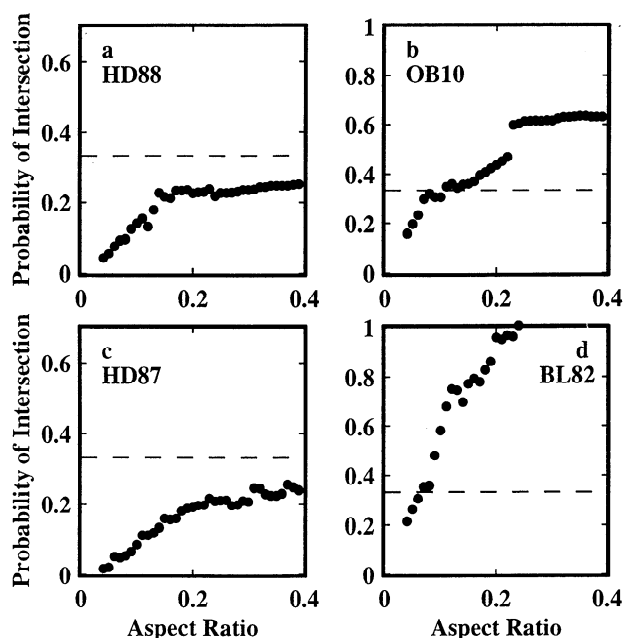
Figure 12. Probability of intersection from equation (5) versus cumulative aspect ratio. The probability of intersection for the melt inclusions of runs (a) HD88 with 1% melt and (c) HD87 with 0.8% melt never reaches the critical probability for the onset of percolation (indicated by the dashed line). (b) Run OB10 with 2.5% melt is right at the percolation threshold, if higher aspect ratio inclusions are disregarded. (d) The intersection probability for run BL82 with 3.3% melt increases rapidly above the critical probability and is about 0.8 at $\alpha_{cut} = 0.15$.

[Stinchcombe, 1974; Essam et al., 1974; Engelman et al., 1983; Gueguen and Dienes, 1989]:

$$f = c\,(p - p_c)^2 \qquad (8)$$

where c is a function of z and p_c and was calculated by Stinchcombe [1974] and Essam et al. [1974] as c = 27 for z = 4 as compared to Gueguen and Dienes' [1989] value of 54. The permeability calculated from (7) and (8) for OB10 at α_{cut} ~ 0.15 (i.e., from all inclusions with an aspect ratio less than 0.15, where the intersection probability p is greater than the critical probability p_c), is k = 7 × 10^{-16} m^2. In comparison, the permeability calculated from (1) with parameters given above (n = 3, C = 100) and the melt fraction in triple junction tubules only ($\phi_T = 0.0014$) is k = 5 × 10^{-20} m^2 (with a mean grain size of OB10 of 41 μm, obtained by multiplying the value in Table 1 by 1.5). The permeability therefore increases by about 4 orders of magnitude on interconnection of the disk-shaped inclusions. For BL82 with a higher melt fraction and greater density of melt inclusions p increases rapidly (Figure 12d), and the calculated permeability at α_{cut} ~ 0.15 is of the order of 10^{-13} m^2.

Discussion

The preceding analysis yields the following view of the interconnectivity of basaltic melt and the permeability of the olivine matrix at low melt fractions: At ϕ ~ 0.001 a network of triple junction tubules with a range of sizes and shapes exists. Small grains are often associated with a large proportion of the total melt fraction. This local melt fraction can exceed the

average melt fraction substantially and typically does not reside in triple junction tubules. An increase in melt fraction is not accommodated by increasing the size of the triple junction tubules; rather, most of the additional melt is stored at two-grain boundaries or larger pools. The size of the triple junction tubules increases somewhat as well, but their proportion of the total melt fraction decreases rapidly to about 10% of the total melt content. Although the triple junction tubules are interconnected, the permeability is low and does not increase substantially with increasing melt fraction.

A comparison of permeabilities calculated from different models emphasizes the significantly lower permeability predicted by this approach up to a melt fraction of 0.02. From equation (1) with $d = 10^{-3}$, $\phi = 0.02$, the predicted permeabilities are: Riley and Kohlstedt [1991] $k = 7 \times 10^{-12}$ m^2 ($n = 1$, $C = 3000$); von Bargen and Waff [1986] $k = 3 \times 10^{-13}$ m^2 ($n = 2$, $C = 1600$); McKenzie [1989] $k = 1 \times 10^{-13}$ m^2 ($n = 2$, $C = 3000$). However, with only 10% of the total melt fraction residing in the tubule network the permeability is $k = 8 \times 10^{-17}$m^2 with $n = 3$, $C = 100$, or lower for $n > 3$. Above $\phi \sim 0.02$ the low aspect ratio melt inclusions interconnect, and as the example above shows, the permeability increases by orders of magnitude. A further increase in melt fraction rapidly increases the fraction of intersecting low aspect ratio inclusions and the permeability, as shown by the comparison of OB10 with BL82.

It is difficult to determine the exact scaling relationship of the melt inclusion parameters with melt fraction and grain size from the present data, since the parameters shown in Table 2 reflect both grain size and melt fraction. For example, although the mean (apparent) grain size of HD88 is almost twice the mean grain size of OB10, the mean length of the low aspect ratio melt inclusions is larger for OB10. This is due to the fact that with increasing melt fraction (2.5 vol. % for OB10 as compared to 1 vol. % for HD88) the number of melt-filled two-grain boundaries increases, and one inclusion can extend over several smaller grains. The same behavior was also observed by Hirth and Kohlstedt [1995a]. The low aspect ratio inclusions are also wider at smaller grain size and higher melt fraction (Table 2). Together these observations indicate that with increasing grain size the melt inclusions become thinner and increase in length.

The inclusions on two-grain boundaries generally are much wider than the melt films predicted for systems with a wetting angle equal to zero [Clarke, 1987]. Hess [1994], based on a model by Clarke [1987], predicted the existence of thin films for anisotropic systems with nonzero wetting angle under certain conditions. These films are of the order of 10 nm thick, below the resolution of backscattered electron imaging. Transmission electron microscope studies of olivine-basaltic melt systems have reported some films of 100 nm and less in thickness [Vaughan et al., 1982; Hirth and Kohlstedt, 1995a, Drury and Fitz Gerald, 1996], whereas the width of the low aspect ratio inclusions discussed in this study ranges from ~0.2 μm to ~5 μm.

The threshold melt fraction at which the low aspect ratio inclusions form an interconnected path was calculated with the assumption of random orientation of these inclusions. It is likely that these inclusions are preferably associated with the most prominent (low index) planes of the equilibrium shape of olivine [Waff and Faul, 1992]. Any preferred alignment of olivine as observed in the ultramafic section of ophiolites [e.g., Nicolas, 1989] and seismic anisotropy measurements [e.g., Nishimura and Forsyth, 1989], or predicted from

modeling of strained olivine aggregates [e.g., Ribe, 1992] will therefore also align the low aspect ratio inclusions. An indication that deformation does not change the general textural features of the partially molten aggregate (the presence of low index olivine planes, completely wetted two-grain boundaries) at least at low stresses and strain rates are experiments by Hirth and Kohlstedt [1995a, b]. Alignment of the disk-shaped inclusions will lower the threshold for interconnection parallel to it.

The concepts of percolation theory have a further implication: right above the percolation threshold, only a few infinite connected clusters exist. A significant amount of melt in clusters not connected to the infinite clusters remains behind (see, for example, Stauffer and Aharony [1992, Chapter 1] for a discussion of this problem in oil fields). If this melt is in the outer regions of the upwelling column at mid-ocean ridges, where the matrix turns horizontal and no further melting occurs, melt can become trapped. This trapped melt could be further stabilized if the melt inclusions are aligned subhorizontally and the vertical permeability is very low. This might help explain broad low-velocity regions observed in seismic studies of mid-ocean ridges [e.g., Forsyth, 1992; Grand, 1994] and perhaps lead to small scale instabilities off axis.

Conclusions

Analysis of the melt distribution in four experiments with olivine and a basaltic melt at elevated pressures and temperatures shows that most of the melt at low melt fractions resides in low aspect ratio, disk-shaped inclusions. The melt distribution is controlled by surface energy minimization in a polycrystalline aggregate in steady state with anisotropic surface energies. The isotropic equilibrium model does not adequately describe the melt distribution in upper mantle rocks, nor does it correctly predict the effects of the melt distribution on bulk physical properties. While tubules along three-grain edge intersections most likely still interconnect the melt at all melt fractions, these tubules are not uniform in size or become uniformly straight at low melt fractions. The amount of melt in tubules is only about 10% of the total melt fraction. Consequently, the permeability of this tubules network is low, and segregation velocities are less than 1 mm yr^{-1}. A substantial increase of the permeability is expected at the melt fraction where the low aspect ratio inclusions on two-grain boundaries first form a connected path.

References

Agee, G. B., and D. Walker, Static compression and olivine flotation in ultrasonic silicate liquid, J. Geophys. Res., 93, 3437-3449, 1988.

Anderson, M. P., G. S. Grest, and D. J. Srolovitz, Computer simulation of normal grain growth in three dimensions, Philos. Mag. B, 59, 293-329, 1989.

Atkinson, H. V., Theories of normal grain growth in pure single phase systems, Acta Metall., 36, 469-491, 1988.

Beere, W., A unifying theory of the stability of penetrating liquid phases and sintering pores, Acta Metall., 23, 131-138, 1975.

Bourbie, T., and B. Zinszner, Hydraulic and acoustic properties as a function of porosity in Fountainebleau sandstone, J. Geophys. Res., 90, 11524-11532, 1985.

Boyd, F. R., and J. L. England, Effect of pressure on the melting of Diopside, CaMgSi$_2$O$_6$, and Albite, NaAlSi$_3$O$_8$, in the range up to 50 kb, *J. Geophys. Res.*, *68*, 311-323, 1963.

Bulau, J. R., H. S. Waff, and J. A. Tyburczy, Mechanical and thermodynamic constraints on fluid distribution in partial melts, *J. Geophys. Res.*, *84*, 6102-6108, 1979.

Bussod, G. Y., and J. M. Christie, Textural development and melt topology in spinel lherzolite experimentally deformed at hypersolidus conditions, *J. Petrol., Special lherzolite issue*, 17-39, 1991.

Charlaix, E., E. Guyon, and N. Rivier, A criterion for percolation threshold in a random array of plates, *Solid State Commun.*, *50*, 999-1002, 1984.

Charlaix, E., E. Guyon, and S. Roux, Permeability of a random array of fractures of widely varying apertures, *Transp. Porous Media*, *2*, 31-43, 1987.

Clarke, D. R., On the equilibrium thickness of intergranular glass phases in ceramic materials, *J. Am. Ceram. Soc.*, *70*, 15-22, 1987.

Cohen, L. H., K. Ito and G. C. Kennedy, Melting and phase relations in an anhydrous basalt to 40 kilobars, *Am. J. Sci.*, *265*, 475-518, 1967.

Cooper, R. F. and D. L. Kohlstedt, Interfacial energies in the olivine-basalt system, in *High Pressure Research in Geophysics, Advances in Earth and Planetary Sciences*, vol. 12, edited by S. Akimoto and M. H. Manghnani, pp. 217-228, Cent. for Acad. Publ. Jpn., Tokyo, 1982.

Cooper, R. F., and D. L. Kohlstedt, Sintering of olivine and olivine-basalt aggregates, *Phys. Chem. Miner.*, *11*, 5-16, 1984.

de Gennes, P. G., *The Physics of Liquid Crystals*, Oxford Univ. Press, New York, 1976.

Dienes, J. K., A statistical theory of fragmentation, in *Proceedings of the 19th U. S. Symposium on Rock Mechanics*, edited by Y. S. Kim, pp. 51-55, Stateline, Nev., 1978.

Dienes, J. K., Permeability, percolation and statistical crack mechanics, in *Issues in Rock Mechanics*, edited by R. E. Goodman and F. E. Heuze, pp. 86-94, Am. Inst. of Min., Metal. and Petrol. Eng., New York, 1982.

Doyen, P. M., Permeability, conductivity, and pore shape evolution of sandstone, *J. Geophys. Res.*, *93*, 7729-7740, 1988.

Drury, M. R., and J. D. Fitz Gerald, Grain boundary melt films in an experimentally deformed olivine-orthopyroxene rock: implications for melt distribution in upper mantle rocks, *Geophys. Res. Lett.*, *23*, 701-704, 1996.

Engelman, R., Y. Gur, and Z. Jaeger, Fluid flow through a crack network in rocks, *J. Appl. Mech.*, *50*, 707-711, 1983.

Essam, J. W., C. M. Place, and E. H. Sondheimer, Selfconsistent calculation of the conductivity in a disordered branching network, *J. Phys. C Solid State Phys.*, *7*, L258-L260, 1974.

Faul, U. H., D. R. Toomey, and H. S. Waff, Intergranular basaltic melt is distributed in thin, elongated inclusions, *Geophys. Res. Lett.*, *21*, 29-32, 1994.

Fisher, M. E., and J. W. Essam, Some cluster size and percolation problems, *J. Math. Phys.*, *2*, 609-619, 1961.

Forsyth, D. W., Geophysical constraints on mantle flow and melt generation beneath mid-ocean ridges, in *Mantle Flow and Melt Generation at Mid-Ocean Ridges, Geophys. Monogr. Ser.*, vol. 71, edited by J. P. Morgan, D. K. Blackman, and J. M. Sinton, pp. 1-65, AGU, Washington, D. C., 1992.

Frank, C. F., Two-component flow model for convection in the Earth's upper mantle, *Nature, 220*, 350-352, 1968.

Grand, S. P., Mantle shear structure beneath the Americas and surrounding oceans, *J. Geophys. Res.*, *99*, 11591-11622, 1994.

Gueguen, Y., C. David, and M. Darot, Models and time constants for permeability evolution, *Geophys. Res. Lett.*, *13*, 460-463, 1986.

Gueguen, Y., and J. K. Dienes, Transport properties of rocks from statistics and percolation, *Math. Geol.*, *21*, 1-13, 1989.

Halperin, B. I., S. Feng, and P. N. Sen, Differences between lattice and continuum percolation transport exponents, *Phys. Rev. Lett.*, *54*, 2391-2394, 1985.

Hess, P. C., Thermodynamics of thin fluid films, *J. Geophys. Res.*, *99*, 7219-7229, 1994.

Hirth, G., and D. L. Kohlstedt, Experimental constraints on the dynamics of the partially molten upper mantle: Deformation in the diffusion creep regime, *J. Geophys. Res.*, *100*, 1981-2001, 1995a.

Hirth, G. and D. L. Kohlstedt, Experimental constraints on the dynamics of the partially molten upper mantle, 2, Deformation in the dislocation creep regime, *J. Geophys. Res.*, *100*, 15441-15449, 1995b.

Hudon, P., D. R. Baker, and P. B. Toft, A high temperature assembly for 1.91-cm (3/4-in.) piston-cylinder apparatus, *Am. Mineral.*, *79*, 145-147, 1994.

Jung, H., U. H. Faul, and H. S. Waff, Crystal size distributions of upper mantle xenoliths and experimentally produced ultramafic partial melts (abstract), *EOS Trans. AGU, 73 (43)*, Fall Meet. Suppl., 502, 1992.

Jurewicz, S. R., and E. B. Watson, The distribution of partial melt in a granitic system: The application of liquid phase sintering theory, *Geochim. Cosmochim. Acta, 49*, 1109-1121, 1985.

Karato, S., Grain growth kinetics in olivine aggregates, *Tectonophysics., 168*, 255-273, 1989.

Kingery, W. D., Effects of microstructure on the properties of ceramics, in *The Physics and Chemistry of Ceramics*, Proceeding of a Symposium Held at the Pennsylvania State University, edited by C. Klingsberg, pp. 286-310, Gordon and Breach, Newark, N. J., 1963.

Laporte, D., Wetting behavior of partial melts during crustal anatexis: The distribution of hydrous silicic melt in polycrystalline aggregates of quartz, *Contrib. Mineral. Petrol.*, *116*, 486-499, 1994.

Laporte, D., and E. B. Watson, Experimental and theoretical constraints on melt distribution in crustal sources: The effect of crystalline anisotropy on melt interconnectivity, *Chem. Geol.*, *124*, 161-184, 1995.

Lesher, C. E., and D. Walker, Cumulate maturation and melt migration in a temperature gradient, *J. Geophys. Res.*, *93*, 10295-10311, 1988.

Lockner, D., and B. Evans, Densification of quartz powder and reduction of conductivity at 700°C, *J. Geophys. Res.*, *100*, 13081-13092, 1995.

Maaløe, S., and A. Scheie, The permeability controlled accumulation of primary magma, *Contrib. Mineral. Petrol.*, *81*, 350-357, 1982.

McKenzie, D., Some remarks on the movement of small melt fractions in the mantle, *Earth Planet. Sci. Lett.*, *95*, 53-72, 1989.

Nicolas, A., *Structures of Ophiolites and Dynamics of Oceanic Lithosphere*, 367 pp., Kluwer Acad., Norwell, Mass., 1989.

Nishimura, C. E., and D. W. Forsyth, The anisotropic structure of the upper mantle in the Pacific, *Geophys. J.*, *96*, 203-229, 1989.

Paterson, M. S., The equivalent channel model for permeability and resistivity in fluid-saturated rock—A re-appraisal, *Mech. Mater.*, *2*, 345-352, 1983.

Ribe, N. M., On the relation between seismic anisotropy and finite strain, *J. Geophys. Res.*, *97*, 8737-8747, 1992.

Riley, G. N., and D. L. Kohlstedt, Kinetics of melt migration in upper mantle-type rocks, *Earth Planet. Sci. Lett.*, *105*, 500-521, 1991.

Russ, J. C., *Computer-Assisted Microscopy: The Measurement and Analysis of Images*, Plenum, New York, 1990.

Stauffer, D., and A. Aharony, *Introduction to Percolation Theory*, Taylor and Francis, Bristol, Pa., 1992.

Stevenson, D. J., On the role of surface tension in the migration of melts and fluids, *Geophys. Res. Lett.*, *13*, 1149-1152, 1986.

Stevenson, D. J., and D. R. Scott, Mechanics of fluid-rock systems, *Annu. Rev. Fluid Mech.*, *23*, 305-339, 1991.

Stinchcombe, R. B., Conductivity and spin-wave stiffness in disordered systems--An exactly soluble model, *J. Phys. C Solid State Phys.*, *7*, 179-203, 1974.

Takahashi, E., Melting of a dry peridotite KLB-1 up to 14 GPa: Implications on the origin of peridotitic upper mantle, *J. Geophys. Res.*, *91*, 9367-9382, 1986.

Turcotte, D. L., and G. Schubert, *Geodynamics*, John Wiley, New York, 1982.

Vaughan, P. J., D. L. Kohlstedt, and H. S. Waff, Distribution of the glass phase in hot-pressed olivine-basalt aggregates: An electron microscope study, *Contrib. Mineral. Petrol.*, *81*, 253-261, 1982.

von Bargen, N., and H. S. Waff, Permeabilities, interfacial areas, and curvatures of partially molten systems: Results of numerical computations of equilibrium microstructures, *J. Geophys. Res.*, *91*, 9261-9276, 1986.

Waff, H. S., and U. H. Faul, Effects of crystalline anisotropy on fluid distribution in ultramafic partial melts, *J. Geophys. Res.*, *97*, 9003-9014, 1992.

Walsh, J. B., and W. F. Brace, The effect of pressure on porosity and the transport properties of rock, *J. Geophys. Res.*, *89*, 9425-9431, 1984.

Zhang, S., M. S. Paterson, and S. F. Cox, Porosity and permeability evolution during hot isostatic pressing of calcite aggregates, *J. Geophys. Res.*, *99*, 15741-15760, 1994.

U. H. Faul, Research School of Earth Sciences, The Australian National University, Canberra ACT 0200, Australia.   (e-mail: uli.faul@anu.edu.au).